Predicting Redesigned Solid Rocket Motor Joint Volume Pressurization, Temperature Transients, and Ablation

Michael O'Malley*
Morton Thiokol, Inc., Brigham City, Utah

A model has been developed to predict volume pressurization, gas and surface temperatures, and erosion due to ablation along a hypothetical leak through the joint insulation and on surfaces with direct hot gas impingement for the redesigned solid rocket motor (RSRM). The overall model is a collection of individual submodels that are composed of analytical and/or empirical equations. To improve confidence in the model, comparisons of pressure, temperature, and erosion predictions with actual test data were performed. Good agreement between the two was found. As a result of this effort, it was discovered that the RSRM O-ring seal design can tolerate major flaws and still function safely. Also, the amount of O-ring erosion is highly dependent on the impingement jet temperature and on the available fill volume in the joint. The model's major contribution to the state of engineering design for high pressure and temperature seals is its use of the differential equation form of Goodman's method for leak-path heat transfer including pulsed heat flux and insulation ablation effects.

Nomenclature

A = surface area for heat transfer
a = cross-sectional flow area
C_H = Stanton number
C_p = heat capacity at constant pressure
C_v = heat capacity at constant volume
d = hydraulic diameter
e = internal energy of O-ring cavity gas
$\bar{f}_F$ = average Fanning friction factor
H = heat-transfer coefficient
H_{stag} = stagnation point heat-transfer coefficient
h = enthalpy
h_D = dissociation enthalpy
h_e = stream enthalpy external to the stagnation point
h_{fg}, h_{fr}, h_{fc} = heat of formation of pyrolysis gas, virgin rubber, and char
$\bar{h}_s$ = enthalpy of ablating wall
K = thermal conductivity
K_T = sum of frictional and form losses for the leak path
L = distance from exit of jet to impingement surface
Le = Lewis number
l = length of flow path
M = mass of gas in O-ring cavity
Ma = Mach number of impinging jet
Ma_{choked} = choking Mach number
$Ma_{unchoked}$ = unchoked Mach number
M_w = molecular weight
$\dot{m}$ = mass flow rate of gas
$\dot{m}_{pygas}$ = pyrolysis gas production rate
P = pressure
P_{motor} = motor pressure
Pr = Prandtl number
Pr_{crit} = critical pressure ratio
Q, Q_{max} = heat flux to leak-path wall and maximum heat flux
$\dot{q}$ = heat transfer from gas to O-ring groove wall
R = gas constant
Re_d = Reynolds number of flow
$\dot{s}$ = erosion rate of material being impinged upon
T = temperature
$T_{abl}, T_{wall}, T_{gas}$ = temperature of insulation ablation, leak-path wall, and ambient gas
T_o = stagnation temperature of gas exiting leak path
T_1, T_2 = wall temperature as a result of constant maximum heat flux, negative temperature added to T_1 to arrive at correct temperature for the decreasing heat flux
U_∞ = jet velocity at nozzle exit
V = volume
W = weighting factor for ablating wall density and heat capacity
X = weighting factor for ablating wall thermal conductivity
x = distance into leak-path wall
α = thermal diffusivity of leak-path walls, $= (K/\rho C_p)$
β = velocity gradient at the stagnation point
δ = distance into wall where thermal gradient goes to zero
δ_1, δ_2 = thermal thickness
γ = specific heat ratio, $= (C_p/C_v)$
μ = viscosity
Ω = fraction of pyrolysis gas to total leak-path gas flow
ϕ = sum of ϕ_h and ϕ_c, which is the mass ratio of motor gas to the total gas in the cavity
ϕ_c = mass ratio of motor gas injected during previous time steps, which has cooled to the cavity gas temperature, to the total gas in the cavity
ϕ_h = mass ratio of motor gas injected during current time step, which is still hot, to the total gas in the cavity
ρ = density

Subscripts

,A = including cooling effects of ablation
air = air

Presented as Paper 88-3332 at the AIAA/SAE/ASME/ASEE 24th Joint Propulsion Conference, Boston, MA, July 11-14, 1988; received Dec. 22, 1988; revision received April 28, 1989.

*Senior Engineer, Aero/Thermal Section. Member AIAA.

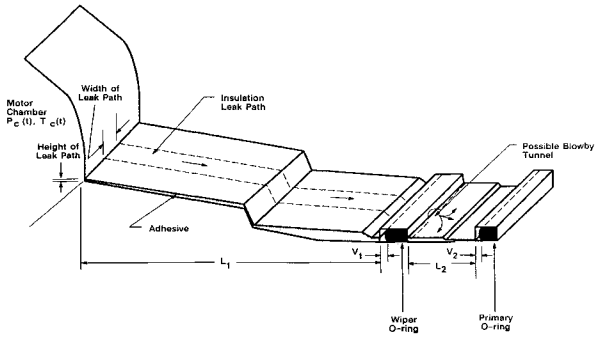

Fig. 1 Typical problem geometry.

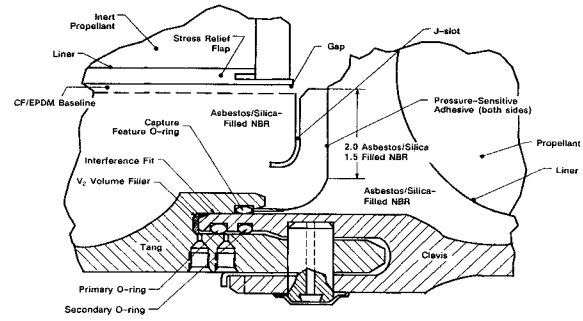

Fig. 2 Case field joint—field joint DM-8 baseline design.

amb	= ambient
cav	= O-ring cavity gas
cg	= cooled motor gas in cavity
char	= char
g	= pyrolysis gas at the ablation temperature
gas	= leak-path gas
in	= hot motor gas entering the cavity
jet	= impinging jet
mix	= cavity gas mixture
,NA	= not including cooling effects of ablation
out	= cavity gas leaving the cavity
path	= leak path
rub	= insulation leak-path wall
vrub	= virgin rubber

Introduction

THE redesigned Space Shuttle solid rocket motor (RSRM) is composed of segments that are held together by pins at the joints. The insulation-to-insulation interface at these joints is bonded together with adhesive. A schematic of the nozzle-to-case joint is shown in Fig. 1. If an insulation-to-insulation debond occurred between the segments, a leak path could exist through which hot chamber gas could flow into the wiper O-ring cavity in the nozzle-to-case joint (Fig. 1) or the capture feature O-ring cavity in the field joint (Fig. 2). This volume-filling process could lead to thermal degradation or erosion of the leak path and O-rings. Erosion on these O-rings is allowed because they are not seals, but it is important to be able to predict how much erosion could occur due to various leak-path sizes. Knowledge of leak-path gas and surface temperatures, leak-path insulation erosion, and volume fill time is also desirable. The volume filling and O-ring erosion problem was studied in the past[1,2]; however, the resulting model was for isentropic flow and used an assumed impingement jet temperature. The present work[3,4] improves on the model by adding friction and compressible flow equations for turbulent, transition, or laminar leak-path flow, and impinging jet and leak-path gas and surface temperatures including ablation. Also improved is cavity heat transfer, including changing wall temperature for turbulent, transition, or laminar circumferential O-ring groove gas flow. Additional improvements are physical properties that are a function of temperature and a dual chamber model that includes all of the features of the single chamber model. This paper will discuss briefly all of these submodels that make up the overall model called ORING2 and will also compare predicted results with test data to validate the modeling.[3,4]

Fundamental Equations

The volume pressurization and mass flow rate equations are fundamental to this study because they allow calculation of the pressure and temperature transients in the cavities and the mass flow rates between them, which in turn provides the O-ring and insulation leak-path erosion predictions. A simple lumped-volume approximation is used because it enables the analyst to study numerous scenarios quickly and economically. The approximation results in some inaccuracy of the average O-ring groove pressure early in the transient but comparable three-dimensional analyses show this to be small. The three-dimensional results show that pressure drops on the order of 10% as it travels around the O-ring groove early in the transient. At later times this pressure drop reduces significantly, improving the approximation.

Volume Pressurization

This model consists of two differential equations for each volume and determines the pressure and temperature transients in each cavity. The rate of change of cavity gas temperature is derived from the conservation of energy equation:

$$\frac{\mathrm{d}(Me)}{\mathrm{d}t} = \dot{m}_{\mathrm{in}} h_{\mathrm{in}} - \dot{m}_{\mathrm{out}} h_{\mathrm{out}} - M\dot{q} - P_{\mathrm{cav}} \frac{\mathrm{d}V_{\mathrm{cav}}}{\mathrm{d}t} \tag{1}$$

This energy balance states that the change in internal energy of the cavity gas is equal to the enthalpy of the incoming gas minus the enthalpy of the outgoing gas, the heat loss to the cavity walls, and the work done changing the volume of gas. Differentiating (Me), assuming the gas is thermally perfect, obtaining an expression for $(\mathrm{d}e/\mathrm{d}t)$ by differentiating the definition of enthalpy, substituting for $(\mathrm{d}e/\mathrm{d}t)$ along with some other substitutions, and solving for $(\mathrm{d}T_{\mathrm{cav}}/\mathrm{d}t)$ yields

$$\frac{\mathrm{d}T_{\mathrm{cav}}}{\mathrm{d}t} = \frac{R_{\mathrm{mix}} T_{\mathrm{cav}}}{P_{\mathrm{cav}} V_{\mathrm{cav}} C_{v_{\mathrm{mix}}}} \left[\dot{m}_{\mathrm{in}} h_{\mathrm{in}} - \dot{m}_{\mathrm{out}} h_{\mathrm{out}} - C_{v_{\mathrm{mix}}} T_{\mathrm{cav}} (\dot{m}_{\mathrm{in}} - \dot{m}_{\mathrm{out}}) - P_{\mathrm{cav}} \frac{\mathrm{d}V_{\mathrm{cav}}}{\mathrm{d}t} \right] - \frac{\dot{q}}{C_{v_{\mathrm{mix}}}} - \frac{R_{\mathrm{mix}} T_{\mathrm{cav}}}{M_{w_{\mathrm{mix}}} C_{v_{\mathrm{mix}}}} \frac{\mathrm{d}M_{w_{\mathrm{mix}}}}{\mathrm{d}t} \tag{2}$$

With $(\mathrm{d}T_{\mathrm{cav}}/\mathrm{d}t)$ known, $(\mathrm{d}P_{\mathrm{cav}}/\mathrm{d}t)$ is derived next. Starting with differentiation of the ideal gas law, solving for $(\mathrm{d}P_{\mathrm{cav}}/\mathrm{d}t)$ and then substituting $(\mathrm{d}M/\mathrm{d}t)$, or the conservation of mass in the cavity, the final expression is

$$\frac{\mathrm{d}P_{\mathrm{cav}}}{\mathrm{d}t} = \frac{R_{\mathrm{mix}} T_{\mathrm{cav}}}{V_{\mathrm{cav}}} (\dot{m}_{\mathrm{in}} - \dot{m}_{\mathrm{out}}) + \frac{P_{\mathrm{cav}}}{T_{\mathrm{cav}}} \frac{\mathrm{d}T_{\mathrm{cav}}}{\mathrm{d}T} - \frac{P_{\mathrm{cav}}}{V_{\mathrm{cav}}} \frac{\mathrm{d}V_{\mathrm{cav}}}{\mathrm{d}T} - \frac{P_{\mathrm{cav}}}{M_{w_{\mathrm{mix}}}} \frac{\mathrm{d}M_{w_{\mathrm{mix}}}}{\mathrm{d}T} \tag{3}$$

If the dual chamber model is being used, Eqs. (2) and (3) are solved for both chambers V_1 and V_2 as shown in Fig. 1.

Mass Flow Rate Model

The mass flow rate of gas into each volume is a function of the Mach number and the flow losses in the leak path. The governing equations were obtained from Ref. 5 and were further developed into their present form in Ref. 6. First, the choking Mach number and critical pressure ratio are calculated. Because of flow losses in the leak path, this choking Mach number, which can occur at a Mach number less than unity, is

$$Ma_{\text{choked}} = \left(\frac{-B - \sqrt{B^2 - 4AC}}{2A}\right)^{1/2} \tag{4}$$

where

$$A = \left(\frac{1}{1 + K_T}\right) - 1$$

$$B = \left[\frac{3}{(1 + K_T)(\gamma - 1)}\right] - \frac{3\gamma - 1}{(\gamma - 1)^2}$$

$$C = \frac{2}{(1 + K_T)(\gamma - 1)^2}$$

The negative root is chosen in the quadratic equation, because A and B are always negative. With the choking Mach number known, the critical pressure ratio is

$$Pr_{\text{crit}} = \left\{1 - \left[\frac{\left(\frac{\gamma - 1}{2}\right)Ma^2_{\text{choked}}}{\left(\frac{1}{1 + K_T}\right)\left[1 + \left(\frac{\gamma - 1}{2}\right)Ma^2_{\text{choked}}\right]}\right]\right\}^{\frac{\gamma}{\gamma - 1}} \tag{5}$$

The iteration to solve for the flow losses and mass flow rate uses the ratio of the cavity pressure to the motor pressure for each time step. If this pressure ratio is less than Pr_{crit}, the choked Mach number is used. If the opposite is true, the flow is unchoked and the unchoked Mach number is needed. The unchoked Mach number is obtained from

$$Ma_{\text{choked}} = \left\{\left(\frac{2}{\gamma - 1}\right)\left(\frac{1}{1 + K_T}\right) \times \left[\frac{1 - (P_{\text{cav}}/P_{\text{motor}})^{\frac{\gamma - 1}{\gamma}}}{1 - [1/(1 + K_T)]\left[1 - (P_{\text{cav}}/P_{\text{motor}})^{\frac{\gamma - 1}{\gamma}}\right]}\right]\right\}^{1/2} \tag{6}$$

The sum of the friction and form losses in the leak path (K_T) is obtained from equations that are described in detail in Ref. 4.

With the appropriate Mach number and the flow losses, the mass flow rate of gas into the cavity can be calculated as follows:

$$\dot{m} = \frac{P_{\text{motor}} a_{\text{jet}}}{\left[\left[\frac{T_o R_{\text{in}}[(\gamma + 1)/2]}{\gamma}\right]^{\frac{\gamma + 1}{\gamma - 1}}\right]^{1/2}} \times \left[\frac{Ma\left[[(\gamma + 1)/2]^{\frac{\gamma + 1}{\gamma - 1}}\right]^{1/2}}{\left[1 + [(\gamma - 1)/2]Ma^2\right]^{\frac{\gamma + 1}{2(\gamma - 1)}}}\right] \times \left[1 - K_T\,[(\gamma - 1)/2]Ma^2\right]^{\frac{\gamma}{\gamma - 1}} \tag{7}$$

As a check, if K_T is set to zero, Eqs. (4–7) revert to the standard insentropic orifice flow equations. Since the total flow loss K_T depends on mass flow rate, Eqs. (4–7) must be solved iteratively.

Leak-Path Heat Transfer

The next important element of the total model is the determination of the heat transfer down the leak path. This requires an ablation model, physical properties of the virgin rubber/char mixture, and the calculation of the leak-path gas temperatures.

Heat Transfer with Ablation Model

A model was needed to calculate how the temperature of the gas changes as it flows down the leak path and impinges on the O-ring. Since ablation of the rubber-insulated walls of the leak path cools the gas significantly, a model was developed to calculate the temperature of the flow-path gas, the exiting jet, and the insulation surface as well as the erosion of the flow path due to ablation.

Increasing Heat Flux

The model is an extension of the integral heat-balance technique pioneered by Goodman,[7] much later summarized by Shadlesky[8] and further developed by Morstadt.[9] The major difference in this work, from previous efforts, is that instead of just conduction and convection occurring at the boundary, it is assumed that the heat required to initiate and sustain ablation and the heat required to increase the pyrolysis gas temperature, from the ablation temperature to the wall temperature, is included and is assumed to occur at the boundary.

Starting with the classical Fourier heat-conduction equation

$$\frac{\partial T}{\partial t} = \alpha\left(\frac{\partial^2 T}{\partial x^2}\right) \tag{8}$$

the boundary conditions are

$$q_{\text{abl}} - q_{\text{cond}} = q_{\text{conv}}, \qquad \text{at } x = 0$$

where

$$q_{\text{abl}} = (h_g - \bar{h}_s)\dot{m}_{\text{rub}} + \dot{m}_{\text{pygas}} C_{p_g}(T_{\text{wall}} - T_{\text{abl}}) \tag{9a}$$

$$q_{\text{cond}} = K_{\text{rub}} A_{\text{path}} \frac{\partial T}{\partial x} \tag{9b}$$

$$q_{\text{conv}} = H_{\text{path}} A_{\text{path}}(T_{\text{gas}} - T_{\text{wall}}) \tag{9c}$$

and

$$T = T_{\text{amb}}, \qquad \frac{\partial T}{\partial x} = 0, \qquad \text{at } x = \delta \tag{10}$$

The variable δ is the depth into the solid where the temperature is approximately the initial temperature. As shown in Eq. (10), this is also the depth where the temperature gradient is assumed to be zero.

The first term on the right side of Eq. (9a) accounts for the heat required to initiate and sustain ablation. The enthalpy of the pyrolysis gas h_g and the solid enthalpy $\bar{h}_s$ are defined as follows:

$$h_g = C_{p_g}(T_{\text{wall}} - T_{\text{amb}}) + h_{fg} \tag{11}$$

$$\bar{h}_s = \frac{\rho_{\text{vrub}}[C_{p_{\text{vrub}}}(T_{\text{abl}} - T_{\text{amb}}) + h_{fr}] - \rho_{\text{char}}[C_{p_{\text{char}}}(T_{\text{abl}} - T_{\text{amb}}) + h_{fc}]}{\rho_{\text{vrub}} - \rho_{\text{char}}} \tag{12}$$

The second term on the right side of Eq. (9a) accounts for the heat required to raise the pyrolysis gas from the ablation temperature to the leak-path wall temperature. The term q_{cond} accounts for the heat conducted into the leak-path wall. As the heat balance shows, all of this heat must come by convection from the gas to the wall.

Integrating Eq. (8) with respect to x, at some fixed time and using Leibnitz's rule and the boundary conditions [Eqs. (9) and (10)], Eq. (8) can be rewritten as

$$\frac{d}{dt}\left(\int_0^{\delta} T\,dx - T_{amb}\delta\right) = \frac{\alpha}{K_{rub}A_{path}}\,[q_{conv} - q_{abl}] \tag{13}$$

The next step is to assume a temperature profile in the solid. The simplest is a quadratic in "x", although a cubic could also have been chosen. Using the boundary conditions, $T(x,t)$ can be derived. When $T(x,t)$ is substituted into the integral of Eq. (13) and integrated, the result is

$$\frac{d}{dt}\left\{\frac{\delta^2}{6K_{rub}A_{path}}\,[q_{conv} - q_{abl}]\right\} = \frac{\alpha}{K_{rub}A_{path}}\,[q_{conv} - q_{abl}] \tag{14}$$

From the temperature profile equations and the fact that, at $x = 0$, $T(x,t)$ equals T_{wall}

$$T_{wall} = T_{amb} + \frac{\delta}{2K_{rub}A_{path}}\,[q_{conv} - q_{abl}] \tag{15}$$

Solving this equation for δ and then substituting for δ and α in Eq. (14), we obtain

$$\frac{dY}{dt} = \frac{d}{dt}\left\{\frac{K_{rub}A_{path}(T_{wall} - T_{amb})^2}{[q_{conv} - q_{abl}]}\right\} = \frac{3}{2}\,\frac{(q_{conv} - q_{abl})}{\rho_{rub}C_{p_{rub}}A_{path}} \tag{16}$$

If a cubic temperature profile had been used, the only change in Eq. (16) would have been the change in the coefficient 3/2 on the right side to 4/3. Solving for T_{wall} as a function of Y using the quadratic equation yields

$$T_{wall} = T_{amb} - \frac{Y}{2K_{rub}}\,(H_{path} + F_{1abl}) + \frac{1}{2}\left[\frac{Y^2}{K_{rub}^2}\,(H_{path} + F_{1abl})^2 - \frac{4Y}{K_{rub}} \times [T_{amb}(H_{path} + F_{1abl}) + F_{2abl} - H_{path}T_{gas} - F_{3abl}]\right]^{1/2} \tag{17}$$

where

$$F_{1abl} = \frac{\dot{m}_{pygas}C_{p_g}}{A_{path}} + \frac{\dot{m}_{rub}C_{p_g}}{A_{path}}$$

$$F_{2abl} = \frac{\dot{m}_{rub}}{A_{path}}\,(h_{fg} - C_{p_g}T_{amb})$$

$$F_{3abl} = \frac{\dot{m}_{pygas}C_{p_g}T_{abl}}{A_{path}} + \frac{\dot{m}_{rub}\bar{h}_s}{A_{path}}$$

Decreasing Heat Flux

As discussed in Ref. 10, the parabolic wall temperature distribution is strictly applicable only when the thermal gradient is positive. Because of the nature of the assumed distribution, if a pulse-like gradient is applied, the parabolic distribution cannot accommodate the decreasing heat flux accurately. For this reason, a modification of the preceding technique is necessary to describe accurately the wall temperature while undergoing a decreasing heat flux. This problem was approached by Goodman[10]; however, his equations were in an integral form that were inconvenient to use. The present method converts those equations to a differential form that can easily be solved using a standard library differential equation solver, DGEAR.

While the heat flux is rising, but prior to its peaking, Eqs. (16) and (17) are used to determine the wall temperature. After reaching the peak, the wall temperature is assumed to consist of two parts.

$$T(x,t) = T_1(x,t) + T_2(x,t) \tag{18}$$

The first is the result of continuing the peak heat flux Q_{max} at a constant level. The surface heat flux associated with the second part is negative and monotonic. Beginning at the moment of peak heat flux, it follows a curve such that the sum of the two parts follows the true boundary condition. Assuming the heat flux is given by Q and its peak value by Q_{max}, and assuming a parabolic temperature distribution in the wall, from Ref. 10,

$$T_1(x,t) = \frac{Q_{max}}{2K_{rub}\delta_1}\,(\delta_1 - x)^2 + T_{amb} \tag{19}$$

$$T_2(x,t) = -\frac{(Q_{max} - Q)}{2K_{rub}\delta_2}\,(x - \delta_2)^2 \tag{20}$$

Here δ_1 is the thermal penetration distance associated with T_1 and δ_2 is the thermal penetration distance associated with T_2. Evaluating Eqs. (19) and (20), at the surface ($x = 0$), and solving for δ_1 and δ_2 yields

$$\delta_1 = \frac{(T_1 - T_{amb})2K_{rub}}{Q_{max}} \tag{21}$$

$$\delta_2 = \frac{-2K_{rub}T_2}{(Q_{max} - Q)} \tag{22}$$

Now an expression that gives Q and Q_{max} as a function of δ_1 and δ_2 is needed, so δ_1 and δ_2 can be eliminated. Again, from Ref. 10,

$$\delta_1 = \sqrt{\frac{6\alpha}{Q_{max}}}\left[\int_0^{t_{max}} Q(t)dt + Q_{max}(t - t_{max})\right]^{1/2}, \quad t > t_{max} \tag{23}$$

and

$$\delta_2 = \sqrt{\frac{6\alpha}{(Q_{max} - Q)}}\left[\int_{t_{max}}^{t} (Q_{max} - Q)\,dt\right]^{1/2}, \quad t > t_{max} \tag{24}$$

The time t_{max} is when Q reaches Q_{max}. Squaring Eq. (23), differentiating both sides with respect to time, and dividing both sides by the thermal conductivity K_{rub}, gives

$$\frac{d}{dt}\left[\frac{\delta_1^2 Q_{max}}{K_{rub}}\right] = \frac{6\alpha Q_{max}}{K_{rub}} \tag{25}$$

Squaring Eq. (24), differentiating both sides with respect to time, using the fundamental theorem of calculus to evaluate the integrals, and dividing both sides by K_{rub}, gives

$$\frac{d}{dt}\left[\frac{\delta_2^2(Q_{max} - Q}{K_{rub}}\right] = \frac{6\alpha}{K_{rub}}\,(Q_{max} - Q) \tag{26}$$

Substituting δ_1 and δ_2 into Eqs. (25) and (26), respectively, yields

$$\frac{dY_1}{dt} = \frac{d}{dt}\left[\frac{(T_1 - T_{amb})^2 K_{rub}}{Q_{max}}\right] = \frac{3}{2}\,\frac{\alpha}{K_{rub}}\,Q_{max} \tag{27}$$

$$\frac{dY_2}{dt} = \frac{d}{dt}\left[\frac{(-T_2)^2 K_{rub}}{(Q_{max} - Q)}\right] = \frac{3}{2}\,\frac{\alpha}{K_{rub}}\,(Q_{max} - Q) \tag{28}$$

Solving for T_1 and T_2 as a function of Y_1 and Y_2, respectively, and substituting T_1 and T_2 into Eq. (18) yields,

$$T_{\text{wall}} = T(0,t) = T_{\text{amb}} + [(Y_1/K_{\text{rub}})Q_{\max}]^{1/2} - [(Y_2/K_{\text{rub}})(Q_{\max} - Q)]^{1/2} \tag{29}$$

The derivation can proceed no further unless Q and $Q_{\max}$ are specified, because Q will probably be a function of $T(0,t)$. Assuming the wall undergoes conduction, convection, and ablation, then

$$Q = q_{\text{conv}}/A_{\text{path}} - q_{\text{abl}}/A_{\text{path}} \tag{30}$$

$$Q_{\max} = [q_{\text{conv}}/A_{\text{path}} - q_{\text{abl}}/A_{\text{path}}]_{\max} \tag{31}$$

The differential equations now become

$$\frac{dY_1}{dt} = \frac{d}{dt}\left[\frac{(T_1 - T_{\text{amb}})^2 K_{\text{rub}}}{(q_{\text{conv}}/A_{\text{path}} - q_{\text{abl}}/A_{\text{path}})_{\max}}\right] = \frac{3}{2}\frac{\alpha}{K_{\text{rub}}}[q_{\text{conv}}/A_{\text{path}} - q_{\text{abl}}/A_{\text{path}}]_{\max} \tag{32}$$

$$\frac{dY_2}{dt} = \frac{d}{dt}\left[\frac{T_2^2 K_{\text{rub}}}{(q_{\text{conv}}/A_{\text{path}} - q_{\text{abl}}/A_{\text{path}})_{\max} - (q_{\text{conv}}/A_{\text{path}} - q_{\text{abl}}/A_{\text{path}})}\right] = \frac{3}{2}\frac{\alpha}{K_{\text{rub}}}[(q_{\text{conv}}/A_{\text{path}} - q_{\text{abl}}/A_{\text{path}})_{\max} - (q_{\text{conv}}/A_{\text{path}} - q_{\text{abl}}/A_{\text{path}})] \tag{33}$$

As before, using the quadratic equation, an expression is derived for T_{wall} as a function of Y_1 and Y_2. The final result is

$$T_{\text{wall}} = T_{\text{amb}} + F_{6\text{abl}} + \frac{Y_2(H_{\text{path}} + F_{4\text{abl}})}{2K_{\text{rub}}} - \frac{1}{2}\left\{\left[2T_{\text{amb}} + 2F_6 + \frac{Y_2(H_{\text{path}} + F_{4\text{abl}})}{K_{\text{rub}}}\right]^2 - 4\left[(T_{\text{amb}} + F_{6\text{abl}})^2 - \left\{\frac{Y_2}{K_{\text{rub}}}\left[\left(\frac{q_{\text{conv}}}{A_{\text{path}}}\right)_{\max} - H_{\text{path}}T_{\text{gas}} + F_{5\text{abl}}\right]\right\}\right]\right\}^{1/2} \tag{34}$$

where

$$F_{4\text{abl}} = \frac{\dot{m}_{\text{pygas}}C_{p_g}}{A_{\text{path}}} + \frac{\dot{m}_{\text{rub}}C_{p_g}}{A_{\text{path}}}$$

$$F_{5\text{abl}} = \frac{\dot{m}_{\text{rub}}}{A_{\text{path}}}(h_{fg} - \bar{h}_s - C_{p_g}T_{\text{amb}}) - \left(\frac{q_{\text{abl}}}{A_{\text{path}}}\right)_{\max} - \frac{\dot{m}_{\text{pygas}}C_{p_g}}{A_{\text{path}}}T_{\text{abl}}$$

$$F_{6\text{abl}} = \frac{Y_1}{K_{\text{rub}}}\left[\frac{q_{\text{conv}}}{A_{\text{path}}} - \frac{q_{\text{abl}}}{A_{\text{path}}}\right]^{1/2}$$

With these equations, the code can predict the temperature of the ablating wall with a pulse-like heat flux applied by solving differential Eqs. (16), (32), and (33) for Y, Y_1 and Y_2. If the wall is not ablating, Eqs. (32–34) can be applied upon setting q_{abl}, $F_{4\text{abl}}$, and $F_{5\text{abl}}$ equal to zero.

A number of unknowns still appear in the preceding equations, and descriptions of the methods used to obtain these values now follow. The first value that is necessary is the Reynolds number along the leak path, taking into account the growth of the leak path due to insulation erosion. Next, the friction term fl/d and heat-transfer coefficient H_{path} are determined for the leak path for this iteration. This heat-transfer coefficient enables the model to determine the total erosion rate of the leak path, including pyrolysis and mechanical erosion, and the erosion due to pyrolysis alone. The erosion correlations were obtained from Refs. 11 and 12.

With the erosion rate of the leak-path wall known, the mass flow rate of pyrolysis gas $\dot{m}_{\text{pygas}}$ and the burnback rate of virgin rubber $\dot{m}_{\text{rub}}$ can be determined. The surface area of the leak path multiplied by the erosion rate gives the volume per second of insulation that is ablating; subsequent multiplication by the density of pyrolysis gas gives the rate of pyrolysis gas being produced. Likewise, this volume multiplied by the density of virgin rubber gives the rate at which virgin rubber is being ablated.

Virgin Rubber/Char Mixture Physical Properties

The leak-path wall is a mixture of virgin rubber and char. Most of its physical properties are relatively insensitive to temperature except the thermal conductivity of the char. For this reason, the char thermal conductivity is evaluated as a function of temperature by using curve-fitted data.

Since the relative amounts of char and virgin rubber present in the thermal layer are not known, an approximate scheme is used to determine them. It is reasoned that the relative amounts are a function of the gas Mach number. The higher the Mach number, the greater the chance of the char layer being blown away and consequently becoming thinner. It is also postulated that, at a Mach number of 0.5, all of the char layer will be gone. Based on this, a weighting factor was defined as

$$W = Ma_{\text{gas}} + 0.5 \tag{35}$$

In terms of this weighting factor, the heat capacity and density of the char/virgin rubber mixture were defined as

$$C_{p_{\text{rub}}} = W(C_{p_{\text{vrub}}}) + (1 - W)\,C_{p_{\text{char}}} \tag{36}$$

and

$$\rho_{\text{rub}} = W(\rho_{\text{vrub}}) + (1 - W)\,\rho_{\text{char}} \tag{37}$$

The thermal conductivity of the mixture is better defined. A density weighting factor is defined as[13]

$$X = \frac{\rho_{\text{rub}} - \rho_{\text{char}}}{\rho_{\text{vrub}} - \rho_{\text{char}}} \tag{38}$$

and the thermal conductivity of the mixture, K_{rub} is

$$K_{\text{rub}} = X(K_{\text{vrub}}) + (1 - X)K_{\text{char}} \tag{39}$$

Flow-Path Gas Temperatures

Other variables needing definition were the gas temperature exiting the leak path and an average gas temperature along the flow path. The gas temperature exiting the leak path, or T_{jet}, was obtained from Shapiro.[14] Assuming the filling process as quasisteady state, so that a constant wall temperature can be assumed for each time step, the equation is

$$T_{\text{jet,NA}} = T_{\text{wall}} + (T_{\text{in}} - T_{\text{wall}})\exp\left(-2\frac{\bar{f}_F l}{d_{\text{path}}}\right) \tag{40}$$

With the inlet motor temperature and the outlet jet temperature known, the integrated average leak-path gas temperature can be derived. This is

$$T_{\text{jet,NA}} = T_{\text{wall}} + \frac{1}{2\bar{f}_F}\left(\frac{d_{\text{path}}}{l}\right)(T_{\text{in}} - T_{\text{jet,NA}}) \tag{41}$$

One final effect of ablation that still needs to be considered is the cooling of the leak-path gas when it mixes with the pyrolysis gases at the cooler wall temperature. This is accomplished by a mass-weighted mixing of the enthalpies of the

leak-path gas and the pyrolysis gas. First, the fraction of pyrolysis gas to total gas flow in the leak path defined as

$$\Omega = \frac{\dot{m}_{\text{pygas}}}{\dot{m}_{\text{gas}}} \tag{42}$$

is calculated. Then the jet temperature and gas temperature are obtained from the following expressions:

$$T_{\text{jet}} = \frac{C_{p_{\text{jet,NA}}} T_{\text{jet,NA}}(1-\Omega) + C_{p_g} T_{\text{wall}}\Omega}{C_{p_{\text{jet,A}}}(1-\Omega) + C_{p_{g,\text{A}}}\Omega} \tag{43}$$

$$T_{\text{gas}} = \frac{C_{p_{\text{gas,NA}}} T_{\text{gas,NA}}(1-\Omega) + C_{p_g} T_{\text{wall}}\Omega}{C_{p_{\text{gas,A}}}(1-\Omega) + C_{p_{g,\text{A}}}\Omega} \tag{44}$$

Equations (43) and (44) state that if all of the leak-path gas is motor gas, that is $\Omega = 0$, then T_{jet} and T_{gas} are not cooled; alternately, if all of the leak-path gas is pyrolysis gas, that is $\Omega = 1$, then T_{jet} and T_{gas} will equal the wall temperature. The denominator of each equation comes from the enthalpy of the mixture, which is at the mixture temperature T_{jet} or T_{gas}. Since they are not yet known for this iteration, the value from the previous iteration is used to calculate the heat capacities of the leak-path gas and pyrolysis gas at the mixture temperature.

Cavity Heat Transfer

To determine the heat transfer from the cavity gas to the surroundings, the cavity surface temperature, the cavity gas mixture physical properties, and the heat-transfer correlations must be defined.

Cavity Surface Temperature Model

To calculate accurately the heat transfer from the cavity gas to the surroundings, the surface temperature of the steel in the O-ring groove must be known. This surface temperature is calculated by using the integral heat-balance technique of Eqs. (16) and (17) after setting q_{abl}, $F_{1\text{abl}}$, $F_{2\text{abl}}$, and $F_{3\text{abl}}$ equal to zero and employing the appropriate subscript changes.

Physical Properties of the Cavity Gas Mixture

To calculate the heat loss from the gas in the cavity, accurate physical properties of the gas mixture in the cavity are essential. This model breaks the mixture up into the following three mass fractions: ϕ_h, ϕ_c, and $(1-\phi)$. By subdividing the gas mixture in this fashion, the effect of changes in composition as well as temperature can be calculated. The equations are

$$M_{w_{\text{mix}}} = \frac{1}{(\phi_h/M_{w_{\text{in}}}) + (\phi_c/M_{w_{\text{cg}}}) + [(1-\phi)/M_{w_{\text{air}}}]} \tag{45}$$

$$\mu_{\text{mix}} = \frac{1}{(\phi_h/\mu_{\text{in}}) + (\phi_c/\mu_{\text{cg}}) + [(1-\phi)/\mu_{\text{air}}]} \tag{46}$$

$$K_{\text{mix}} = \phi_h K_{\text{in}} + \phi_c K_{\text{cg}} + (1-\phi) K_{\text{air}} \tag{47}$$

$$C_{p_{\text{mix}}} = \phi_h C_{p_{\text{in}}} + \phi_c C_{p_{\text{cg}}} + (1-\phi) C_{p_{\text{air}}} \tag{48}$$

These mixture formulas are derived from a dimensional analysis.

Cavity Heat-Transfer Correlations

In the cavity heat-transfer model, each domain of flow is described by its own equation. If the cavity flow is turbulent, the Petukov equation is used to determine the cavity heat-transfer coefficient.[15] If the cavity Reynolds number is within the transition between turbulent and laminar flow, a linear interpolation between the value of the turbulent heat-transfer coefficient evaluated at the turbulent Reynolds number cutoff and the value of the laminar heat-transfer coefficient evaluated at the laminar Reynolds number cutoff is made. Currently, this is the best alternative because there is no available, very reliable correlation in the transition zone. If the cavity Reynolds number is in the laminar region, one of two equations can be used; the Nusselt equation for fully developed flow or the laminar Sieder and Tate equation that includes entrance effects.[15]

The heat transferred from the cavity gas to the O-ring groove steel walls is obtained using these heat-transfer coefficients and the surface temperature and area of the exposed steel. This heat flux is used in determining the cavity pressure and temperature.

O-ring Erosion

An O-ring can undergo blowby and/or jet impingement erosion. If an insulation flaw is present and the O-ring remains sealed, jet impingement erosion can occur. If the seal fails allowing gas past it, the O-ring will endure blowby as well as jet impingement erosion.

Jet Impingement Erosion Model

The development of the jet impingement erosion model is discussed in detail in Ref. 3. Briefly, the jet impingement erosion rate depends on the stagnation-point heat-transfer coefficient, which in turn depends on the velocity gradient at the stagnation point. This can be expressed as the ratio of jet velocity decay to jet radius decay. The decays are a function of the nozzle-to-plate spacing or the distance from the outlet of the jet to the impingement surface.

Various correlations for compressible and incompressible axisymmetric jet velocity decay, jet radius decay, and stagnation-point velocity gradient were studied. The velocity gradient correlations chosen for the potential core region and the transition region were obtained from Ref. 16. The velocity gradient for the fully turbulent region was obtained by taking the ratio of the compressible axisymmetric jet velocity decay[17] to the compressible axisymmetric jet radius decay.[18] with the velocity gradient at the stagnation point known, various correlations for stagnation-point heat-transfer coefficient were studied and compared. The one chosen[19] provided the closest matching of data and was applicable for hot compressible gas flow including dissociation effects. An equation for axisymmetric laminar jets was also found.[20] Finally, an experimental correlation relating Viton erosion rate with stagnation-point heat-transfer coefficient was developed using least-squares linear regression from char motor data resulting in the values for C_1 and C_2. The final erosion model can be summarized by displaying the equations. First, the Stanton number is calculated

For $Re_{d_{\text{jet}}} < 1000$:

$$C_H = 0.763\, Pr^{-3/5} \left(\beta \frac{d_{\text{jet}}}{U_\infty}\right)^{1/2} \left(Re_{d_{\text{jet}}}\right)^{-1/2} \left(\frac{T_{\text{jet}}}{T_{\text{abl}}}\right)^{0.1667} \tag{49}$$

For $L/d_{\text{jet}} \le 12$:

$$\left(\beta \frac{d_{\text{jet}}}{U_\infty}\right) = 1.0 \tag{50}$$

For $Re_{d_{\text{jet}}} > 1000$:

$$C_H = 0.442\, Pr^{-3/5} \left(\beta \frac{d_{\text{jet}}}{U_\infty}\right)^{1/2} \left(Re_{d_{\text{jet}}}\right)^{-1/2} \left(\frac{T_{\text{jet}}}{T_{\text{abl}}}\right)^{0.03333} \times \left(\frac{2L}{d_{\text{jet}}}\right)^{1/2} \left[1 + (Le^{0.52} - 1)\frac{h_D}{h_e}\right] \tag{51}$$

For $L/d_{\text{jet}} \le 2.6$:

$$\left(\beta \frac{d_{\text{jet}}}{U_\infty}\right) = 1.0 \tag{52}$$

For $2.6 < L/d_{jet} < 8.4$:

$$\left(\beta \frac{d_{jet}}{U_\infty}\right) = -0.038\left(\frac{L}{d_{jet}}\right) + 1.13 \tag{53}$$

For $L/d_{jet} \geq 8.4$:

$$\left(\beta \frac{d_{jet}}{U_\infty}\right) = \frac{1 - \exp\left[\dfrac{-1.0}{\left(\dfrac{L}{d_{jet}}\right)\left(\dfrac{0.7407}{3.2 + 1.1Ma^2}\right) - 0.7407}\right]}{0.13\left(\dfrac{L}{d_{jet}}\right) - 0.39} \tag{54}$$

Then the relationship between heat-transfer coefficient and erosion rate is used, shown by the following expressions:

$$\frac{H_{stag}}{C_{p_{jet}}} = \rho_{jet} U_\infty C_H \tag{55}$$

$$\dot{s} = C_1\left(\frac{H_{stag}}{C_{p_{jet}}}\right)^{C_2} \tag{56}$$

where $C_1 = 70.715$ and $C_2 = 0.6$

Equation (56) does not include the effect of jet temperature directly, so it would predict Viton erosion even when the jet is below the ablation temperature of 1265°R. A simple correction remedies this problem. The above correlation is strictly applicable at a jet temperature equal to the flame temperature (6203°R) of the burning propellant in the test section of the char motor, but should predict no erosion at a jet temperature less than the ablation temperature. Drawing a straight line between these two points produces

$$\dot{s}_{corrected} = \left(\frac{\dot{s}}{4937.4}\right) T_{jet} - 0.25629\ (\dot{s}) \tag{57}$$

With the erosion rate for this time step, the total accumulated erosion is obtained from

$$s_{accumulated} = s_{old} + \dot{s}_{corrected}\ (\Delta t) \tag{58}$$

Blowby Erosion Model

The blowby erosion model is similar to the leak-path erosion model. The heat-transfer coefficient is calculated for turbulent, transition, or laminar flow using the same heat-transfer equations as described previously for pipe flow. Using the same correlation of $H/C_{p_{jet}}$ vs erosion rate as used for jet impingement erosion of the O-ring, the blowby tunnel erosion rate is obtained and summed over time to obtain the total erosion depth. This erosion rate is also used to calculate the growth of the height and width of the blowby tunnel during each time step.

Results

To provide verification that the model correctly describes volume filling pressurization and erosion, comparisons were made between test data and calculated values. Predictions without plugging and data matching with plugging were performed using data from the 70-lb charge subscale motor tests. In addition, predictions and matching of data from the nozzle joint environment simulator (NJES) and the joint environment simulator (JES) tests were performed.

70-lb Charge Motor

To study the structural and thermal effects of different J-joint insulation and O-ring flaws on the RSRM field joint and to gain data for model verification, a series of subscale motors employing 70 lb of shuttle propellant each were fired. The 70-lb charge motor test section duplicates the full-scale field joint in cross section; however, the motor diameter is only 7% of the full-scale RSRM diameter. Initial attempts to model the 70-lb subscale motor results used constant flow-path dimensions; however, they were unsuccessful because the leak path erodes, growing larger in cross-sectional area with time. In addition, the leak path plugs up with char and aluminum oxide particles, sometimes gradually, sometimes suddenly. The larger concentration of particles present in the leak-path gas stream in a 70-lb motor may be because upstream of the joint ablating inert propellant is present, rather than burning propellant, as in a full-scale motor. To describe this effect, a plugging model was developed that related the reduction in leak-path dimensions with the volume of the incoming particles.[21] One drawback of the equation was that the particle mass concentration in the leak-path gas stream was assumed and could change radically and unpredictably throughout the firing. This unknown history of particle mass concentration makes the plugging model of limited usefulness for predicting tests, but it can be used to match existing test data quite well.

Of the 23 test motors fired in phase 1, eight tests (13–20) employed intentional flaws in the demonstration motor eight (DM-8) J-Joint (Fig. 2), which has a slightly different insulation design than the RSRM design. The results of these eight tests were predicted using ORING2,[3,4] assuming constant leak-path dimensions. In all cases, the predicted erosion exceeded the measured erosion due to the shortened fill time as a result of plugging. Analysis of all eight tests using the plugging model is planned, but at the present time only results for tests 13 and 15 have been compared with predictions. Figures 3–5 show results for the matching of test 13. For this matching, a composite motor pressure trace was calculated by averaging the values from tests 13–18 and using this as the driving pressure. The actual thermocouple data for jet temperature in the leak-path flaw was used as the impingement temperature. Comparisons were made between runs using constant jet dimensions and runs using the leak-path burnback and pluggage model described previously. Figure 3 compares predicted and measured cavity pressure transients along with the averaged motor pressure transient for a constant jet width. Figure 4 shows the improvement in the predicted cavity pressure transient when the leak path is allowed to ablate. The jet width grows initially to a predicted value of 0.272 in., due to insulation ablation. This compares well with the actual burned out minimum jet width of 0.32 in. To match the actual O-ring erosion however, the leak path must begin to plug so that the dimensions get smaller and the jet becomes more concentrated. According to the test data, the cavity and motor pressure begin to diverge, indicating complete pluggage by 2.8 s. At approximately 0.35 s, or the point where the cavity is very close to being filled, the Mach number in the flow path falls to a very low value, signaling the beginning of plugging, because at the low gas velocity the particles can precipitate out of the gas stream much easier. The mass concentration of particles in the flow stream down the leak path was set at 30%. The jet width and height continue to reduce until 2.8 s when the height becomes zero, totally closing off the leak path. This burning out and plugging scenario results in a very close matching of the cavity pressure transient, the jet width burnout, and the predicted O-ring erosion of 55.8 mil compared to the measured value of 55.4 mil. A comparison of the O-ring erosion transients for test 13 is shown in Fig. 5.

Test 15 was also matched using the burning out and plugging model for variable jet width and height. However, for test 15 to match the volume pressurization and the measured O-ring erosion, the mass concentration of particles had to be set at 67% from 1–1.6 s and then 3% after 1.6 s. Unlike test 13, which showed a more gradual buildup of particles blocking the leak path, test 15 suggests a quick blockage followed by much slower buildup, which never really blocks the leak path totally. This highlights what was brought out before;

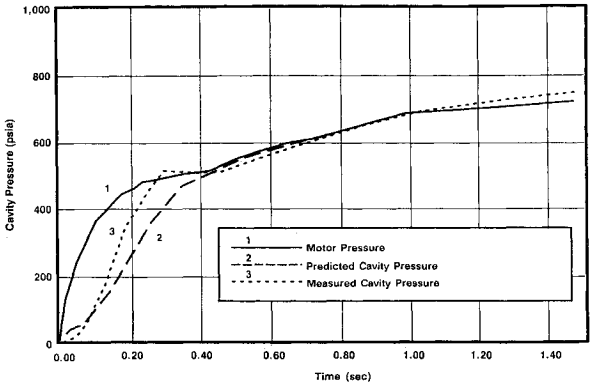

Fig. 3 Cavity pressure vs time (test no. 13; constant width = 0.25).

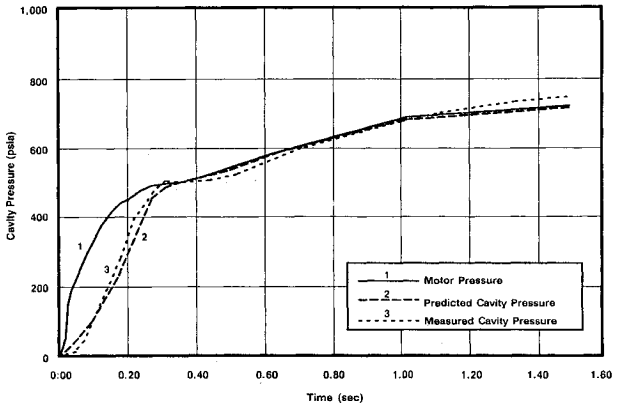

Fig. 4 Cavity pressure vs time (test no. 13; variable width).

predicting plugging may be impossible due to large changes in the mass concentration of particles in the leak-path gas stream. The O-ring erosion prediction of 105.9 mil for test 15 using variable jet dimensions is very close to the actual measured erosion of 105.0 mil. For both cases, cavity pressure, insulation erosion, and O-ring erosion were accurately matched using the burning out and plugging model.

NJES Test Motor

The NJES test motor is designed to simulate the pressurization and temperature transients during ignition in addition to testing insulation and 0-ring seal flaws in a full-scale RSRM nozzle-to-case joint, shown in Fig. 1, of the full-scale motor. The test motor is a short stack constructed by attaching a full-scale forward dome to a full-scale aft dome, eliminating the motor segments normally in between. Propellant slabs and a full-scale RSRM igniter provide the combustion gas. NJES-1A data was matched using ORING2 for purposes of model validation. The analysis used the measured NJES-1A motor pressure trace and a motor temperature trace predicted by an ignition transient code. The width of the intentional insulation leak path was 0.35 in. and the average height was 0.16 in. The code predicted 47 mil of jet impingement erosion for the primary O-ring, which compared well with the actual measured erosion of 45 mil. Figure 6 compares the predicted primary O-ring cavity pressure transient with data from two test gauges. Again the agreement is good. This example shows that ORING2 can predict accurately volume pressurization and O-ring erosion.

JES Test Motor

Similar to the NJES is the JES series of tests. They are designed to simulate the full-scale field joint pressurization

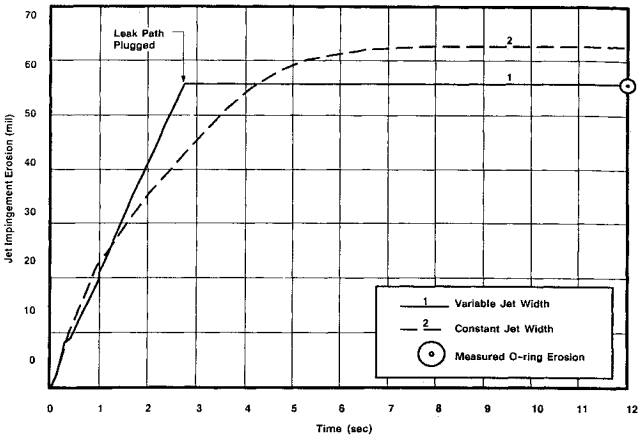

Fig. 5 Jet impingement erosion vs time (test no. 13; variable vs constant jet width = 0.25).

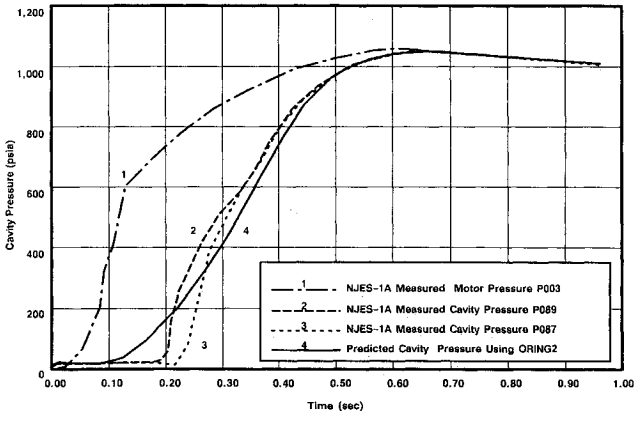

Fig. 6 NJES-1A motor pressure: predicted and actual cavity pressure transients (insulation flaw: 0.35 × 0.16 in.).

and temperature transients during ignition and to study insulation and O-ring seal flaws. This test motor, like the NJES test motor, is also a short stack but this time constructed from a full-scale forward dome and two full-scale motor segments, eliminating the nozzle-to-case joint. This provides two full-scale field joints, A and B, on which to obtain data as a result of induced flaws. As before, propellant slabs and a full-scale RSRM igniter provide the combustion gas. Joint A of JES-3B had an intentional 0.125 × 0.05 in. insulation flaw in the DM-8 style J-joint shown in Fig. 2. This was designed to form an impinging jet on the capture feature O-ring during joint pressurization. The motor pressure was not allowed to vent in an attempt to keep the temperature and pressure close to that in a real motor. Predictions,[22] including capture feature O-ring erosion, were made with the ORING2 model. Assuming the J-joint initially closes and stays closed due to good adhesive bonding, the total predicted capture feature O-ring erosion was 150 mil. The absence of soot circumferentially in the J-joint radius of the test hardware, outside of the defect itself, indicates that was the case. The predicted capture feature O-ring erosion of 150 mil compares well with the measured erosion of 137 mil.

Conclusions

As a result of this modeling effort, it was discovered that the RSRM O-ring seal design can tolerate major flaws and still function safely. It was also learned that the amount of O-ring erosion is highly dependent on the impingement jet temperature and on the available fill volume in the joint,

which determines the amount of time the jet impinges on the O-ring. Another conclusion is that the heat loss through an insulation leak path due to ablation is substantial and its calculation essential to providing an accurate impingement jet temperature.

The benefit of this model is its ability to analyze quickly and economically numerous failure modes without resorting to costly and time-consuming testing. This can be done because the model's predictive capability has been compared with test data. The model's major contribution to the state of engineering design for high pressure and temperature seals is its use of the differential equation form of Goodman's method for leak-path heat transfer including pulsed heat flux and insulation ablation effects. Because of the assumed in-depth temperature distribution this method uses, it can provide accurate leak-path surface temperatures during high gas temperature transients without resorting to detailed nodalization within the solid. In addition, the use of the library differential equation solver DGEAR provides the capability to add more detail to the model as the need arises. There are a number of limitations to the modeling capability, however. For example, no in-depth material temperature data are calculated, only surface temperatures. The model only outputs an average cavity temperature so the circumferential temperature gradient along the O-ring groove is unknown. And, although the top and bottom of the leak path can be different materials, these materials must be used for the entire length of the leak path.

References

[1]Salita, M., "Prediction of Pressurization and Erosion of the SRB Primary O-Rings During Motor Ignition (Part I): Model Development and Validation," Morton Thiokol, Inc., Brigham City, UT, Thiokol/Wasatch Rept. TWR-14952, April 1985.

[2]Salita, M., "Prediction of Pressurization and Erosion of the SRB Primary O-Rings During Motor Ignition (Part II): Parametric Studies of Field and Nozzle Joints," Morton Thiokol, Inc., Brigham City, UT, Thiokol/Wasatch Rept. TWR-15186, June 1985.

[3]O'Malley, M., "ORING2: Volume Filling and O-Ring Erosion Prediction Code, Improved Model Descriptions and Validation (Part I): Improved O-Ring Erosion Model," Morton Thiokol, Inc., Brigham City, UT, Thiokol/Wasatch Rept. TWR-17030, Aug. 1985.

[4]O'Malley, M., "ORING2: Volume Filling and O-Ring Erosion Prediction Code, Improved Model Descriptions and Validation (Part II): Improved Volume Filling Model and Code Validation," Morton Thiokol, Inc., Brigham City, UT, Thiokol/Wasatch Rept. TWR-17031, Nov. 1987.

[5]Zucrow, M. H. and Hoffman, J. D., *Gas Dynamics,* Vol. 1, Wiley, New York, 1976, pp. 210–219.

[6]Morstadt, R., "Orifice Model for Space Shuttle O-Ring Tests," Morton Thiokol, Inc., Brigham City, UT, Thiokol Memo 2814-FY85-M047, Sept. 1984.

[7]Goodman, T. R., "The Heat-Balance Integral and Its Application to Problems Involving a Change of Phase," *Transactions of the ASME,* Vol. 80, Feb. 1958, pp. 335–342.

[8]Shadlesky, P., "Solution of the Fourier Conduction Equation by the Integral Heat-Balance Technique," Morton Thiokol, Inc., Brigham City, UT, Thiokol Memo 2815-81-M092-1001, Sept. 1981.

[9]Morstadt, R., "Nozzle/Case Joint Redesign Flow/Thermal Analysis, Appendix B," Morton Thiokol, Inc., Brigham City, UT, Thiokol/Wasatch Rept. TWR-17016 Rev. A, Nov. 1987.

[10]Goodman, T. R., (ed.), "Application of Integral Methods to Transient Nonlinear Heat Transfer," *Advances in Heat Transfer,* Vol, 1, Academic, New York, 1964, pp. 52–56, 85–96.

[11]Pendleton, S. B., "Evaluation of Elastomeric Insulation Materials at High Chamber Pressures," Morton Thiokol, Inc., Brigham City, UT, Thiokol/Wasatch Rept. TWR-3896, March 1970.

[12]Koehler, L., "Preliminary Method for Predicting V44/V45 Insulation Material Loss Due to Circumferential Flow," Morton Thiokol, Inc., Brigham City, UT, Thiokol Memo L213-FY87-M103, May 1987.

[13]Clever, R. M. and Denny, V. E., "Response of Charring Ablators to Severe Aerodynamic and Erosion Environments," *Journal of Spacecraft and Rockets,* Vol. 12, Sept. 1975, pp. 558–564.

[14]Shapiro, A. H., *The Dynamics and Thermodynamics of Compressible Fluid Flow,* Parts I and II, Ronald Press, New York, 1958, pp. 243–244.

[15]Chapman, A. J., *Heat Transfer,* 4th ed., MacMillan, New York, 1984, pp. 280–284.

[16]Tani, I. and Komatsu, Y., "Impingement of a Round Jet on a Flat Surface," *Proceedings of the 11th International Congress of Applied Mechanics,* Springer-Verlag, Munich, 1966, pp. 672–676.

[17]Lau, J. C., "Mach Number and Temperature Effects on Jets," *AIAA Journal,* Vol. 18, June 1980, pp. 609–610.

[18]Wilson, R. A. M. and Danckverts, P. V., "Studies in Turbulent Mixing: Part II, A Hot-Air Jet," *Chemical Engineering Science,* Vol. 19, 1964, pp. 885–895.

[19]Comfort, E. H., O'Connor, T. J., and Cass, L. A., "Heat Transfer Resulting from the Normal Impingement of a Turbulent High Temperature Jet on an Infinitely Large Flat Plate," *Proceedings of the Heat Transfer and Fluid Mechanics Institute,* Stanford Univ. Press, Stanford, CA, June 1966, pp. 44–62.

[20]Shadlesky, P. S., "Stagnation-Point Heat Transfer for Jet Impingement to a Plane Surface," *AIAA Journal,* Vol. 21, Aug. 1983, pp. 1214–1215.

[21]Ahmad, R. and Morstadt, R., "Nozzle Boot Cavity Pressurization," Morton Thiokol, Inc., Brigham City, UT Thiokol/Wasatch Rept. TWR-18034, Jan. 1988.

[22]O'Malley, M. J., "Jet Impingement Erosion Predictions for JES-3B, Joint A," Morton Thiokol, Inc., Brigham City, UT, Thiokol Memo L213-FY88-M057, Sept. 1987.